

UNIVERSIDADE ESTADUAL DE CAMPINAS
SISTEMA DE BIBLIOTECAS DA UNICAMP
REPOSITÓRIO DA PRODUÇÃO CIENTÍFICA E INTELLECTUAL DA UNICAMP

Versão do arquivo anexado / Version of attached file:

Versão do Editor / Published Version

Mais informações no site da editora / Further information on publisher's website:

<https://journals.aps.org/prd/abstract/10.1103/PhysRevD.90.024035>

DOI: 10.1103/PhysRevD.90.024035

Direitos autorais / Publisher's copyright statement:

©2014 by American Physical Society. All rights reserved.

DIRETORIA DE TRATAMENTO DA INFORMAÇÃO

Cidade Universitária Zeferino Vaz Barão Geraldo

CEP 13083-970 – Campinas SP

Fone: (19) 3521-6493

<http://www.repositorio.unicamp.br>

Circular geodesics of naked singularities in the Kehagias-Sfetsos metric of Hořava's gravity

Ronaldo S. S. Vieira,^{1,2,3,*} Jan Schee,^{3,†} Włodek Kluźniak,^{2,3,‡} Zdeněk Stuchlík,^{3,§} and Marek Abramowicz^{2,3,4,||}

¹*Instituto de Física “Gleb Wataghin,” Universidade Estadual de Campinas,
13083-859 Campinas, São Paulo, Brazil*

²*Copernicus Astronomical Center, ulica Bartycka 18, PL-00-716 Warszawa, Poland*

³*Institute of Physics, Faculty of Philosophy and Science, Silesian University in Opava,
Bezručovo nám. 13, CZ-74601 Opava, Czech Republic*

⁴*Physics Department, Gothenburg University, SE-412-96 Göteborg, Sweden*

(Received 21 November 2013; published 14 July 2014)

We discuss photon and test-particle orbits in the Kehagias-Sfetsos (KS) metric of Hořava's gravity. For any value of the Hořava parameter ω , there are values of the gravitational mass M for which the metric describes a naked singularity, and this is always accompanied by a vacuum “antigravity sphere” on whose surface a test particle can remain at rest (in a zero angular momentum geodesic), and inside which no circular geodesics exist. The observational appearance of an accreting KS naked singularity in a binary system would be that of a quasistatic spherical fluid shell surrounded by an accretion disk, whose properties depend on the value of M , but are always very different from accretion disks familiar from the Kerr-metric solutions. The properties of the corresponding circular orbits are qualitatively similar to those of the Reissner-Nordström naked singularities. When event horizons are present, the orbits outside the Kehagias-Sfetsos black hole are qualitatively similar to those of the Schwarzschild metric.

DOI: 10.1103/PhysRevD.90.024035

PACS numbers: 04.50.Kd, 04.70.Bw, 04.40.Dg, 95.10.Eg

I. INTRODUCTION

Hořava [1,2] proposed a quantum theory that is invariant under Lifshitz scaling ($t \rightarrow \beta^z t$, $x \rightarrow \beta x$), with the dynamical critical exponent z flowing from $z = 3$ in the short wavelength limit, to the value $z = 1$ in the IR limit. The theory “could therefore serve as a UV completion of Einstein's general relativity” [1]. Gravity is an emergent property of the IR limit of the theory; for instance, Newton's constant is given by a constant of the theory, κ , through $G = \kappa^2/(32\pi c)$, c being the speed of light. See [3,4] for a further development of this quantum theory of gravity.

Kehagias and Sfetsos (KS) [5] showed that the action, if suitably modified [by adding the last term in Eq. (2)] is compatible with Minkowski vacuum, and allows a spherically symmetric, asymptotically flat metric solution. The KS solution [5] was reviewed in many papers (e.g., [6,7]). Here, we give a brief summary of the result. Writing the metric in the form

$$ds^2 = -N^2 dt^2 + g_{ij}(dx^i + N^i dt)(dx^j + N^j dt) \quad (1)$$

and discarding the cosmological term, the authors of Ref. [5] considered the action

$$S = \int dt d^3x \sqrt{g} N \left\{ \frac{2}{\kappa^2} (K_{ij} K^{ij} - \lambda K^2) - \frac{\kappa^2}{2\nu^4} C_{ij} C^{ij} + \frac{\kappa^2 \mu}{2\nu^2} \epsilon^{ijk} R_{i\ell}^{(3)} \nabla_j R^{(3)\ell}_k - \frac{\kappa^2 \mu^2}{8} R_{ij}^{(3)} R^{(3)ij} + \frac{\kappa^2 \mu^2}{8(1-3\lambda)} \frac{1-4\lambda}{4} (R^{(3)})^2 + \mu^4 R^{(3)} \right\}, \quad (2)$$

where $K_{ij} = (\dot{g}_{ij} - \nabla_i N_j - \nabla_j N_i)/(2N)$ is the extrinsic curvature of the $t = \text{const}$ hypersurfaces and $C^{ij} = \epsilon^{ikm} \nabla_k (R^{(3)j}_m - R^{(3)} \delta^j_m/4)$ is the Cotton tensor, $R^{(3)}$ being the 3-D Ricci scalar of the hypersurfaces. The constants κ , ν and λ are dimensionless, while the constant μ has mass dimension 1. The terms involving ν vanish in the spherically symmetric case [5]. Recently, the properties of binary pulsars were used to put general constraints on actions of this type [8].

Kehagias and Sfetsos [5] obtained a spherically symmetric solution which is asymptotically flat in the $\lambda = 1$ case, with $N_i = 0$, and $N^2 = 1/|g_{rr}| \equiv f$, where f is given by Eq. (5). The obtained solution contains the parameter $\omega = 16\mu^2/\kappa^2 > 0$, in addition to the gravitational mass M , and tends to the Schwarzschild solution in the limit of large values of the dimensionless parameter product ωM^2 (expressed in geometrized units). Presumably, ω is a universal constant, if the solution found in [5] correctly describes the gravity of spherically symmetric objects. For large masses, $\omega M^2 > 1/2$, the Kehagias-Sfetsos solution has event horizons; i.e., it corresponds to a black hole [5]. The current observational (lower) limits on ω are not

*ronssv@ifi.unicamp.br

†jan.schee@fpf.slu.se

‡wlodek@camk.edu.pl

§zdenek.stuchlik@fpf.slu.se

||marek.abramowicz@physics.gu.se

particularly stringent [9–12], and are compatible with the existence of naked singularities at masses $M < 2.6 \times 10^4 M_\odot$.

In this paper we discuss the circular geodesics of the KS solution, basing our work on the KS metric, Eq. (4) below, in which the gravitating object is either a black hole or a naked singularity, depending on its gravitational mass (once the Hořava parameter, ω , is fixed at any value).

Circular timelike geodesics are, of course, of great astronomical interest, predating even the birth of physics. Currently they play a fundamental role not only in investigations of planetary motion, but also in the dynamics of galaxies and of the brightest x-ray sources, such as quasars and x-ray binaries, where the emissions are powered by accretion disks. The properties of accretion disks, such as their luminosity, photon spectrum, time variability and the possible presence of an inner edge of the disk close to the ISCO (innermost stable circular orbit) are all intimately related to the properties of circular orbits of the accreting fluid [13–17]. The astrophysical information is carried from the disk to the observer by photons traveling through the cosmic vacuum, so null geodesics are of great interest as well. Further, circular photon orbits, present already in the Schwarzschild solution to Einstein’s general relativity (GR), may leave behind an observable time signature [18,19], so it is important to clarify whether or not circular photon orbits exist for the KS black holes and naked singularities.

Testing GR and alternative theories of gravity provides an additional motivation for the current study. Geodesics around KS black holes have already been studied [6,20–22], with naked singularity geodesics mentioned in Ref. [22], as well as circular motion and accretion disks in slowly rotating extensions of the KS spacetime in [7]. The similarity of general properties of black hole geodesics in GR and in the KS metric has been pointed out in Ref. [6]. However, as we find below, geodesics around naked KS singularities have different properties from those in the Kerr metric.

For any value of ω , a sufficiently small M value will allow the naked singularity KS solution. Properties of geodesics, and hence also of accretion disks, around naked singularities and black holes may be quite different, as is already known from studies in the GR context [23]. As we will see, there are quite striking differences in the properties of circular geodesics between black holes and naked singularities in the KS metric as well. If the properties of the observed stellar mass black hole candidates turn out to be incompatible with the theoretical properties of the KS naked singularities, this will allow placing a stringent lower limit on the value of the Hořava parameter (Sec. VIII). Accordingly, we focus on the orbital properties of the KS spacetime in the naked singularity case. Similar investigations were recently carried out for the Reissner-Nordström metric [24,25], and a remarkable qualitative similarity

between the properties of the circular geodesics of naked singularities in that GR metric and in the KS metric of Hořava’s gravity is one of the conclusions of our paper.

II. KS SPACETIME

The KS solution corresponds to a spherically symmetric, static metric

$$ds^2 = g_{tt}dt^2 + g_{rr}dr^2 + g_{\theta\theta}d\theta^2 + g_{\varphi\varphi}d\varphi^2, \quad (3)$$

and has the form [5]

$$ds^2 = f(r)dt^2 - f^{-1}(r)dr^2 - r^2(d\theta^2 + \sin^2\theta d\varphi^2), \quad (4)$$

with

$$f(r) = 1 + r^2\omega \left[1 - \left(1 + \frac{4M}{\omega r^3} \right)^{1/2} \right]. \quad (5)$$

The Schwarzschild solution $f(r) = 1 - 2M/r$ is recovered in the limit of $\omega \rightarrow \infty$. Further insight into the properties of the metric may be gleaned from embedding diagrams [26].

At first sight there are two parameters in the metric coefficients, ω and M . In fact, the KS metric depends on a single parameter alone, the combination ωM^2 . Indeed, in terms of $x \equiv r/M$,

$$f(x) = 1 - \omega M^2 x^2 \left[\left(1 + \frac{4}{\omega M^2 x^3} \right)^{1/2} - 1 \right]. \quad (6)$$

For convenience, we extend the domain to include $x = 0$, where we take $f(0) = 1$. Note that f is continuous and $f \leq 1$ for all $x \geq 0$. The behavior of f can be seen in Fig. 1,

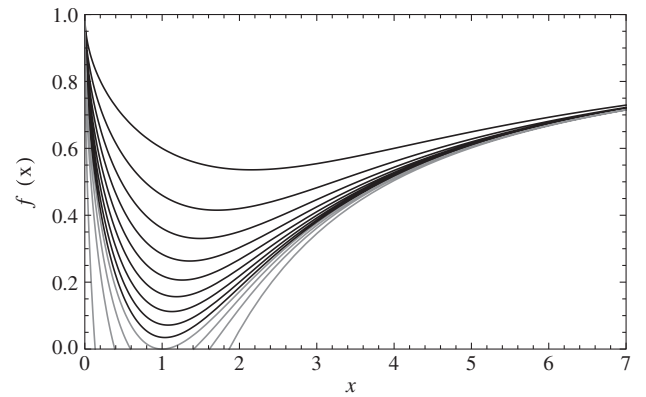


FIG. 1. The g_{tt} coefficient of the KS metric. For $L = 0$, this is also the effective potential $V_{\text{eff}} = f$, given by Eq. (23). For the black curves (positive everywhere), corresponding to naked singularities, ωM^2 varies from 0.05 to 0.45 in steps of 0.05, from the higher to the lower curve; for the gray curves (having zeros), corresponding to black holes, ωM^2 has the values 0.5, 0.6, 0.8, and 2.0, increasing in the same sense. The function $f \leq 1$ satisfies $f \rightarrow 1$ as $x \rightarrow 0^+$ and $x \rightarrow \infty$, and is continuous everywhere. The zeros of f correspond to the radial location of the event horizons.

for different values of ωM^2 . As $f \equiv g_{tt}$ here, $f = 0$ corresponds to the presence of an event horizon. This occurs [5] for $\omega M^2 \geq 1/2$, with two horizons present for all $\omega M^2 > 1/2$.

It is interesting to ask whether with the current limits on ω the observed astrophysical black holes would be black holes or naked singularities in the KS metric. The value of ω has been constrained via solar system tests to be $\omega > 9.1 \times 10^{-26} \text{ cm}^{-2}$ [11], and $\omega > 3.2 \times 10^{-20} \text{ cm}^{-2}$ [12]. The latter, more stringent, constraint implies that no KS naked singularities can exist with mass exceeding $2.6 \times 10^4 M_\odot$. Thus, in principle, stellar-mass black hole candidates of mass $M \sim 10 M_\odot$ in the so-called micro-quasars could be naked KS singularities (they could also be KS black holes if the actual value of ω is much larger than the best lower limit). However, the $4 \times 10^6 M_\odot$ Sgr A* source at the center of the Galaxy would necessarily be a black hole.

If the true value of ω is sufficiently low to preclude the existence of $\sim 20 M_\odot$ black holes ($\omega < 0.5 \times 10^{-13} \text{ cm}^{-2}$), one expects that core collapse of stars massive enough to form a black hole in GR would instead form a naked singularity in the KS metric. While such a collapse has not yet been computed in Hořava's gravity, no other end point of such a collapse has been envisaged.

The issue of primordial black holes is also worthy of note. For any value of ω , at sufficiently low value of M a black hole solution is impossible in the KS metric. Thus, the smallest primordial “black holes” would not be black holes at all, but naked singularities, and thus would escape Hawking evaporation. In fact no black hole could evaporate in a finite time in the KS metric because the Hawking temperature of KS black holes would go to zero at the lower mass limit [27]: $T_H \rightarrow 0$ as $\omega M^2 \rightarrow 1/2$.

For $\omega M^2 < 1/2$ the KS solution has an interesting feature, which distinguishes it from naked singularity solutions in GR: g_{tt} is finite everywhere. The metric coefficients are continuous at $r = 0$, with $f(0) = 1$. However, their radial derivatives are not finite: $f'(x) \rightarrow \infty$ as $x \rightarrow 0$, and this leads to a singularity in the curvature [5].

The radial acceleration of a static timelike observer is given by

$$a_r = \frac{1}{2f} f'(r). \quad (7)$$

The general properties of the KS metric imply that this acceleration vanishes at a certain radius in the naked singularity case ($\omega M^2 < 1/2$). Indeed, since f is continuous and $f(0) = 1$, $f(\infty) = 1$, it follows that there will be a radius at which $f' = 0$. Further, as $f \leq 1$, this radius corresponds to a minimum of f (Fig. 1), and this is a stable equilibrium position of any test particle. This radius, r_{0G} , at which $a_r = 0$, could be termed the “antigravity radius.” Its value is

$$x_{0G} \equiv r_{0G}/M = (2\omega M^2)^{-1/3}. \quad (8)$$

The angular momentum and frequency of $r = \text{const}$ geodesics also vanish at r_{0G} . Below this radius the radial acceleration of a static observer points inwards and therefore there are no circular timelike geodesics; this is the case of repulsive gravity (antigravity). Thus, circular geodesics exist only for $r > r_{0G}$, and there are also stable timelike geodesics corresponding to rest at $r = r_{0G}$.

III. EQUATORIAL GEODESIC MOTION

To fix the notation we begin with a brief review of circular motion in a spherically symmetric, static metric, with signature $(+---)$. For geodesics we have the following constants of motion:

$$E \equiv g_{tt} \dot{t} = u_t, \quad (9)$$

$$L \equiv -g_{\phi\phi} \dot{\phi} = -u_\phi, \quad (10)$$

respectively, the energy and angular momentum of a test particle. From these conserved quantities we can construct the *specific* angular momentum, also conserved,

$$\ell \equiv \frac{L}{E} = -\frac{u_\phi}{u_t}. \quad (11)$$

For circular equatorial geodesics ($r = \text{const}$, $\theta = \pi/2$), we may write the squared specific angular momentum $\ell^2(r)$ in terms of the angular velocity Ω :

$$\ell^2(r) = \tilde{r}^4 \Omega^2(r), \quad (12)$$

where (e.g., [16])

$$\tilde{r}^2 = -\frac{g_{\phi\phi}}{g_{tt}} \quad (13)$$

and

$$\Omega^2(r) = -\frac{\partial_r g_{tt}}{\partial_r g_{\phi\phi}}. \quad (14)$$

A. Timelike circular geodesics

The radial dependence of timelike equatorial geodesic motion is described by the equation

$$E^2 = -g_{tt} g_{rr} \dot{r}^2 + V_{\text{eff}}(r), \quad (15)$$

where the *effective potential* is defined by

$$V_{\text{eff}} = \left(1 - \frac{L^2}{g_{\phi\phi}}\right) g_{tt}. \quad (16)$$

From $\partial V_{\text{eff}}/\partial r = 0$ we obtain the angular momentum of circular geodesics:

$$L^2(r) = -\frac{g_{\varphi\varphi}g_{tt,r}}{g_{tt}g_{\varphi\varphi,r} - g_{\varphi\varphi}g_{tt,r}}. \quad (17)$$

This formula was obtained in [28] by a direct analysis of the geodesic equations.

The second derivative of the effective potential is related to the stability of circular motion. Indeed, $\partial^2 V_{\text{eff}}/\partial r^2$ evaluated at the circular orbit is proportional to the radial epicyclic frequency and hence its sign determines whether or not the Rayleigh criterion is satisfied [16]. This can also be seen from the relation

$$\left. \frac{\partial^2 V_{\text{eff}}}{\partial r^2} \right|_{\text{circ}} = \frac{g_{tt,r}}{L^2(r)} \frac{dL^2(r)}{dr}, \quad (18)$$

valid in the equatorial plane circular orbits of any static, axially symmetric spacetime. For timelike circular geodesics, $E(r)$ and $L(r)$ satisfy a precise relation [28] $dL^2/dr = \tilde{r}^2 dE^2/dr$, and hence $\ell^2(r)$ and $L^2(r)$ satisfy

$$\frac{d\ell^2(r)}{dr} = \frac{1}{E^2} (1 - [\tilde{r}\Omega(r)]^2) \frac{dL^2(r)}{dr}. \quad (19)$$

Thus, for $r > r_{0G}$ the sign of $\partial^2 V_{\text{eff}}/\partial r^2$ is the same as that of $d\ell^2(r)/dr$ and of $dL^2(r)/dr$. As is well known, radial stability corresponds to $d\ell^2(r)/dr > 0$, or equally to $dL^2(r)/dr > 0$, while radial instability corresponds to $d\ell^2(r)/dr < 0$, i.e. to $dL^2(r)/dr < 0$. The term in brackets in Eq. (19) is recognized as the particle's circular velocity measured by a local static observer, $v^2 = \tilde{r}^2 \Omega^2$.

B. Null circular geodesics

The motion of photons in the equatorial plane is described by the equation

$$\frac{E^2}{L^2} = -g_{tt}g_{rr} \frac{\dot{r}^2}{L^2} + V_{\text{ph}}(r), \quad (20)$$

with the effective potential

$$V_{\text{ph}} = -\frac{g_{tt}}{g_{\varphi\varphi}} = \frac{1}{\tilde{r}^2}. \quad (21)$$

The condition for a circular photon orbit is $\partial V_{\text{ph}}/\partial r = 0$. Maxima of V_{ph} correspond to radially unstable photon orbits, whereas minima of V_{ph} correspond to stable photon orbits. From (13), (17), and (21) we see that in any static, axially symmetric spacetime $L^2(r) \rightarrow \infty$ as the radius of the circular timelike geodesic approaches that of the photon orbit.

IV. GEODESIC MOTION IN KS SPACETIME

In KS spacetime, with the metric given by Eqs. (4) and (5), we have

$$V_{\text{ph}} = \frac{f}{r^2} \quad (22)$$

$$V_{\text{eff}} = f(r) \left(1 + \frac{L^2}{r^2} \right), \quad (23)$$

$$L^2(r) = \frac{r^3 f'(r)}{2f - r f'}, \quad (24)$$

$$\ell^2(r) = \left(\frac{r^3}{2f^2} \right) f'(r), \quad (25)$$

$$\Omega^2(r) = \frac{f'(r)}{2r}. \quad (26)$$

The allowed regions for circular timelike motion have qualitatively different properties, depending on the value of ωM^2 , as summarized in Fig. 3. This figure shows the antigravity radius x_{0G} (solid line), the marginally stable orbits x_{ms} (dotted lines) and the photon orbits x_{ph} (dot-dashed lines). We also show the different regions of stability for circular timelike geodesics: stable region (dark gray), unstable region (light gray) and “forbidden” regions where no circular geodesics are allowed (white). There are two such forbidden regions: one between the two photon orbits (at lower values of ωM^2) or between the outer horizon and the unstable photon orbit (at higher values of ωM^2), and one where static observers suffer an inward radial acceleration (either the region $x < x_{0G}$, at lower values of ωM^2 , or the one between the singularity and the inner horizon, at higher values of ωM^2). The behavior of $L^2(r)$ is depicted in Fig. 4; note the correspondence of the curves with the stability regions presented in Fig. 3. Since the spacetime is spherically symmetric, all circular timelike geodesics are vertically stable.

The photon radii in KS spacetime are positive solutions of the equation

$$x_{\text{ph}}^3 - 9x_{\text{ph}} + \frac{4}{\omega M^2} = 0, \quad (27)$$

and the two photon orbits merge at

$$(\omega M^2)_{\text{ms,ph}} = \frac{2}{3\sqrt{3}} = 0.384900, \quad (28)$$

for $x_{\text{ms,ph}} = \sqrt{3}$. An interesting feature of photon orbits in the KS naked singularity spacetime is that the inner photon orbit is stable. This fact can be seen directly from the behavior of V_{ph} , Eq. (22), and it is illustrated in Fig. 2. Related to this fact is a potentially relevant astrophysical consequence: for values of ωM^2 which admit the stable photon orbit there is also an inner region of stable timelike circular geodesics, as depicted in Fig. 3. This region of stability (with respect to both radial and vertical perturbations) extends from x_{0G} to the inner photon radius.

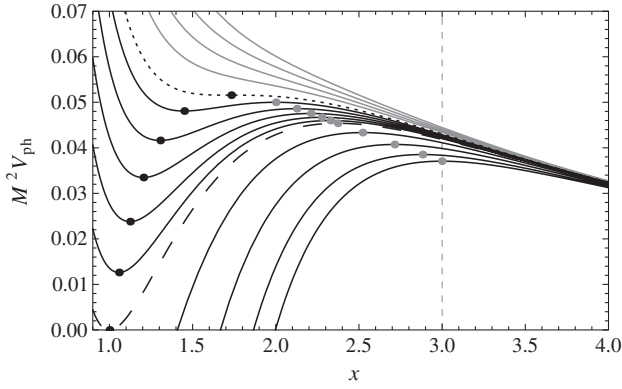


FIG. 2. Effective potential for photons at the equatorial plane, Eq. (22). Different curves correspond to different values of ωM^2 . The upper, gray curves have $\omega M^2 = 0.30, 0.32, 0.34, 0.36$, from top to bottom. They do not allow circular photon orbits. The black short-dashed curve corresponds to $(\omega M^2)_{\text{ms,ph}}$, Eq. (28). The positive black curves have ωM^2 varying from 0.40 to 0.48 in steps of 0.02 and correspond to the naked singularity case. The dashed black curve corresponds to $\omega M^2 = 0.5$. The black curves below it have $\omega M^2 = 0.6, 0.9, 2.0$ and 100. Black dots correspond to stable photon orbits, whereas gray dots correspond to unstable photon orbits. The black dot on the short-dashed curve represents the marginally stable photon orbit. The vertical dashed line at $x = 3$ marks the Schwarzschild value of the photon orbit radius.

The point $(\sqrt{3}, 2\sqrt{3}/9)$ on the $x-\omega M^2$ plane, at which the stable and unstable circular photon orbits merge into the marginally stable photon orbit, Eq. (28), is also the termination point of the locus of the marginally stable timelike orbits, as can be seen in Fig. 3. For $\omega M^2 < (\omega M^2)_{\text{ms,ph}}$ there are no photon orbits. It can be shown that this “joining” is a general feature for metrics of the

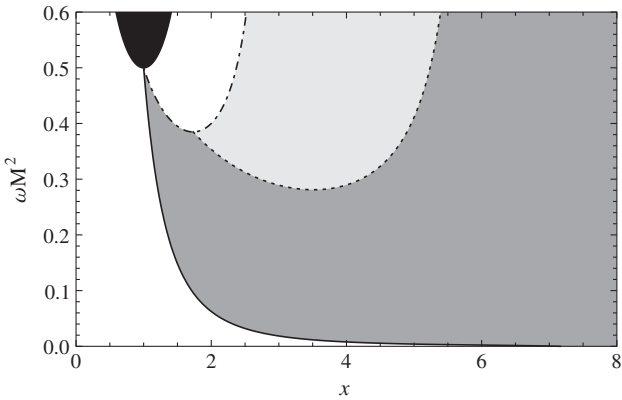


FIG. 3. Regions of (in)stability of timelike circular geodesics and relevant radii in the KS spacetime. Black: Region between horizons, where the vector ∂_t is spacelike. Dark gray: Stability region for timelike circular geodesics. Light gray: Instability region for timelike circular geodesics. White: Region of no circular timelike geodesics. Solid line: x_{0G} . Dotted lines: x_{ms} . Dot-dashed lines: x_{ph} . We see that the x_{ms} line meets the photon orbit lines, at $(x_{\text{ms,ph}}, (\omega M^2)_{\text{ms,ph}})$; see Eq. (28).

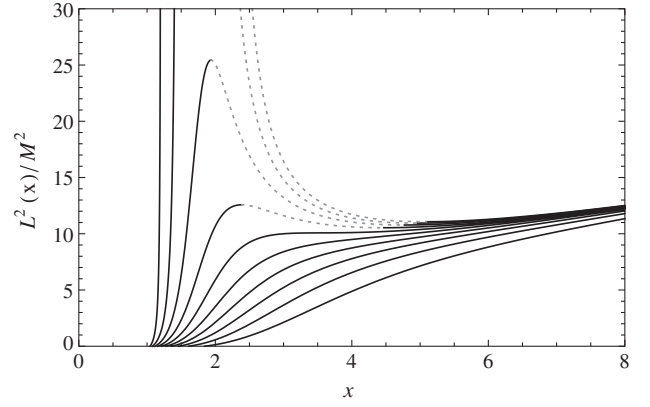


FIG. 4. Angular momentum (squared) of test particles in circular orbits as a function of x . Different curves are for different values of ωM^2 , varying from 0.08 (bottom) to 0.44 (top) in steps of 0.04. Solid black lines correspond to stable motion, whereas dotted gray lines correspond to unstable motion. The lower six curves correspond to the case of no marginally stable orbits, $\omega M^2 < (\omega M^2)_{\text{ms}}$. The next two (middle) curves, for $(\omega M^2)_{\text{ms}} < \omega M^2 < (\omega M^2)_{\text{ms,ph}}$, exhibit two marginally stable orbits, an ISCO and an OSCO. For the upper two curves, $(\omega M^2)_{\text{ms,ph}} < \omega M^2$, the angular momentum in the inner stable branch goes to infinity at the stable photon orbit, and the angular momentum in the unstable branch goes to infinity at the unstable photon orbit. There are no circular orbits between the photon orbits. See Sec. IV and Fig. 3.

form (4), namely, that if a curve of marginally stable circular orbits “touches” a curve of photon orbits, then it should do it precisely at a marginally stable photon orbit. By Eqs. (17) and (21), we have $L^2(r) = -g_{tt,r}/(\partial_r V_{\text{ph}})$. The marginally stable orbits ($dL^2/dr = 0$) then satisfy

$$g_{tt,rr} = g_{tt,r} \frac{\partial_r^2 V_{\text{ph}}}{\partial_r V_{\text{ph}}}. \quad (29)$$

Since $g_{tt,rr}$ and $g_{tt,r}$ are finite at the photon orbits, the quotient $\partial_r^2 V_{\text{ph}}/\partial_r V_{\text{ph}}$ must be finite at the photon orbit where the marginally stable curve “reaches.” But at photon orbits $\partial_r V_{\text{ph}} = 0$, and thus we must have $\partial_r^3 V_{\text{ph}} = 0$ at the “triple point,” which is the condition for a marginally stable photon orbit (assuming that $\partial_r^3 V_{\text{ph}} \neq 0$).

For $(\omega M^2)_{\text{ms}} < \omega M^2 < (\omega M^2)_{\text{ms,ph}}$, with $(\omega M^2)_{\text{ms}} = 0.281100$, there are two marginally stable orbits among the timelike circular geodesics. The inner one, at radius r_{OSCO} could be termed the outermost stable circular orbit (OSCO) as for all r satisfying $r_{0G} < r < r_{\text{OSCO}}$ there are stable circular orbits, while the outer one, at r_{ISCO} , present for all $\omega M^2 > (\omega M^2)_{\text{ms}}$ is the ISCO familiar from the Schwarzschild metric, as there are stable circular orbits for all $r > r_{\text{ISCO}}$. Thus, there are two regions of stability of circular test-particle motion for $(\omega M^2)_{\text{ms}} < \omega M^2 < (\omega M^2)_{\text{ms,ph}}$. The OSCO and ISCO coincide for $\omega M^2 = (\omega M^2)_{\text{ms}}$. For $\omega M^2 < (\omega M^2)_{\text{ms}}$ all circular orbits are stable down to x_{0G} .

This situation is analogous to the inner stability regions found in Reissner-Nordström naked-singularity spacetimes [25] and Reissner-Nordström spacetimes with a cosmological constant [24]. An example is also known (in nonlinear electrodynamics) of regular spacetimes in which the same qualitative scenario appears [29].

V. THE EFFECTIVE POTENTIAL FOR TEST PARTICLES

In this section, we systematically discuss the behavior of V_{eff} for test-particle motion in terms of ωM^2 .

For the black hole case ($\omega M^2 > 1/2$) the situation is analogous to the Schwarzschild metric (Fig. 5). For sufficiently high values of angular momentum $V_{\text{eff}}(r)$ has a maximum at r_{unst} , corresponding to an unstable circular orbit, and a minimum at r_{st} , corresponding to a stable circular orbit. At a certain critical value of angular momentum, L_{ms} , the two extrema merge at the radius r_{ms} of the marginally stable circular orbit. The unstable, marginally stable, and stable orbit radii satisfy $r_{\text{unst}} < r_{\text{ms}} < r_{\text{st}}$. Hence, in this case the marginally stable orbit is an ISCO. For $L < L_{\text{ms}}$ no circular orbits are possible.

The remaining three cases (Figs. 6, 8, 7) correspond to naked singularities. If $(\omega M^2)_{\text{ms,ph}} < \omega M^2 < 1/2$ the spacetime admits two photon orbits, which correspond to the $L^2 \rightarrow \infty$ limit of test-particle orbits (see Figs. 2, 4). This is indeed the situation for the first two extrema of V_{eff} (Fig. 6). As L^2 increases without bounds, both the (first local) minimum and maximum values of $V_{\text{eff}}(r)$ increase without bounds. The marginally stable orbit appears (at a radius larger than that of the unstable photon orbit) at a radius at which $L^2(r)$ reaches a (locally) minimum value, which we will denote by $L_{\text{ms}}^2(\omega M^2)$. Note that a stable circular orbit is always present between x_{0G} and the stable photon orbit, while the unstable circular orbit and the

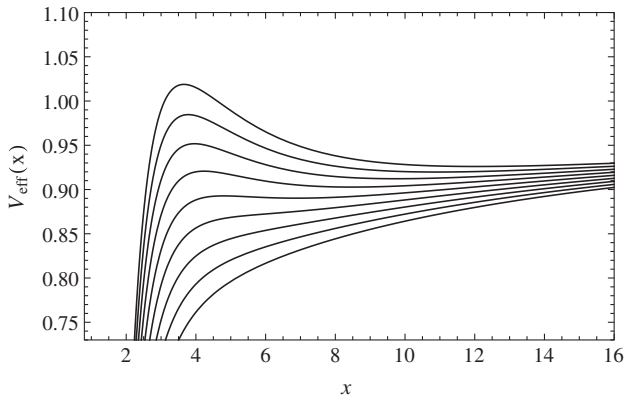


FIG. 5. Effective potential V_{eff} as a function of x for different values of L^2 (decreasing from top to bottom). Depicted in the figure is the KS black hole case, $\omega M^2 = 1 > 1/2$, qualitatively similar to the Schwarzschild solution.

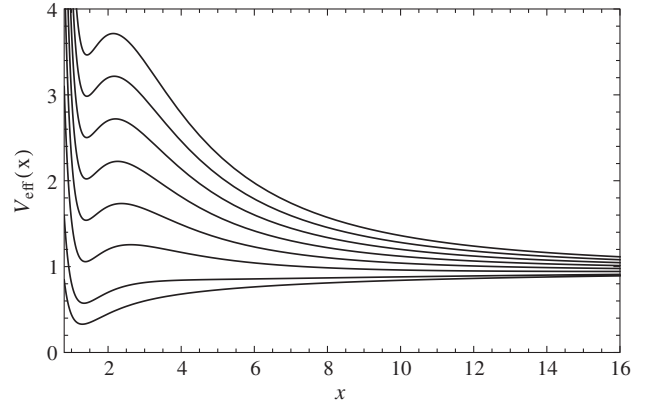


FIG. 6. Same as Fig. 5, but for $(\omega M^2)_{\text{ms,ph}} < \omega M^2 = 0.4 < 0.5$, the regime with two photon orbits and one marginally stable orbit.

second (familiar) stable circular orbit (both at radii larger than that of the unstable photon orbit) are present only for values of $L^2 > L_{\text{ms}}^2$.

We note that the behavior of V_{eff} for high angular momentum, as shown in Fig. 6, is not a particular feature of the KS naked-singularity solution, but instead a property of geodesic motion. If there is a local maximum of V_{eff} at $r_{\text{unst}}(L^2)$ for every high value of L^2 and if this sequence of radii has a bounded limit as $L^2 \rightarrow \infty$, this limit will correspond to an unstable circular photon orbit. In the same way, if there is a local minimum of V_{eff} at $r_{\text{st}}(L^2)$ for every high value of L^2 and if this sequence of radii has a bounded limit as $L^2 \rightarrow \infty$, this limit will correspond to a stable circular photon orbit.

If we now consider $(\omega M^2)_{\text{ms}} < \omega M^2 < (\omega M^2)_{\text{ms,ph}}$ there still are two separate regions of stability, but no photon orbit (Fig. 3). We see from Fig. 8 that the inner stable orbit is present for low values of L^2 , but as the magnitude of angular momentum is increased a marginally stable orbit is reached (the OSCO; see Fig. 4), and at higher values still of $|L|$ only the familiar outer stable orbits persist. Conversely, the outer stable orbits exist only for values of $|L|$ larger than the value in the ISCO. The unstable circular orbits exist only in a range of L^2 values, merging with the outer stable circular orbit at the lower end of the range (corresponding to the ISCO) and with the inner circular orbit at the higher end of the range (corresponding to the OSCO).

The last case is $\omega M^2 < (\omega M^2)_{\text{ms}}$, for which the situation is analogous to the familiar motion in Newtonian gravity at $x > x_{0G}$. Figure 7 shows that in this regime there is only one circular orbit for each value of angular momentum, and this orbit is stable. The orbits extend down to x_{0G} , which plays the role of the radius of a Newtonian star, or planet. However, it would be misleading to expect that the properties of the orbits as a function of their radius are the same as those of Keplerian orbits

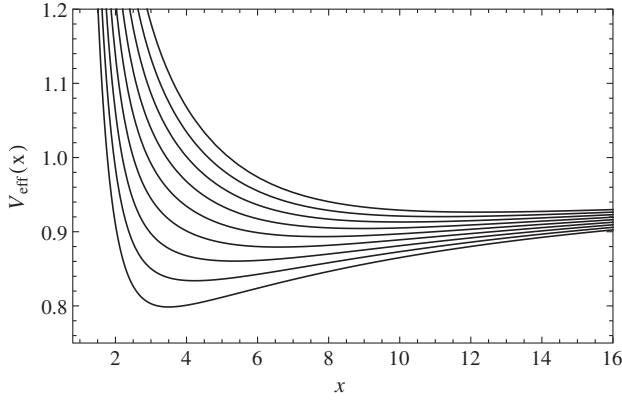


FIG. 7. Same as Fig. 5, but for $\omega M^2 = 0.2 < (\omega M^2)_{\text{ms}}$, the regime of stable orbits alone, qualitatively similar to Newtonian gravity for $x > x_{0G}$; cf. Eq. (8).

in a Newtonian $1/r$ potential, where the orbital frequency monotonically increases with r . This cannot be the case here, as the angular frequency of the orbits goes to zero at both edges of the allowed domain, $\Omega \rightarrow 0$ equally for $r \rightarrow \infty$ and $r \rightarrow r_{0G}$, implying that the (positive) angular frequency (squared) has a maximum. This is indeed the case, as can be seen in Fig. 9, which shows $\Omega^2(r)$. We will denote the radius at which the maximum of $\Omega^2(r)$ occurs by $r_{\Omega \text{ max}}$.

The profiles of the angular frequency $\Omega(x)$, given by Eq. (26), in the three naked-singularity regimes defined by the values of $\omega M^2 < 1/2$, are all similar. $\Omega^2(x)$ is always a curve with a zero at the antigravity radius x_{0G} ; it then monotonically increases, passes through a maximum—except for $(\omega M^2)_{\text{ms,ph}} < \omega M^2 < 1/2$, when there is a region without circular orbits, so the domain of Ω^2 is not simply connected—and decreases monotonically tending to zero at infinity, $\Omega(x) \rightarrow 0$ for $r \rightarrow \infty$. For $(\omega M^2)_{\text{ms}} < \omega M^2 < 1/2$, a part of the curve corresponds to unstable orbits (dotted lines in Fig. 9).

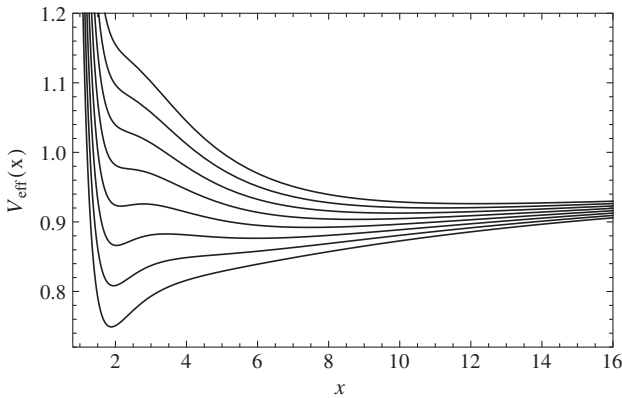


FIG. 8. Same as Fig. 5, but for $(\omega M^2)_{\text{ms}} < \omega M^2 = 0.32 < (\omega M^2)_{\text{ms,ph}}$, the regime with two marginally stable orbits.

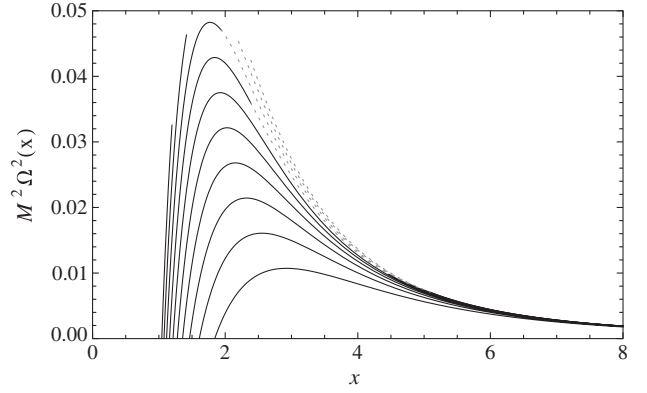


FIG. 9. Angular frequency of the circular orbits as a function of x . Different curves are for different values of ωM^2 in the naked-singularity regime, varying from 0.08 (bottom) to 0.44 (top) in steps of 0.04. Solid black lines correspond to stable motion, whereas dotted gray lines correspond to unstable motion in the region between the OSCO and the ISCO (or the photon orbit and the ISCO, for the top two curves).

VI. DISCUSSION OF ACCRETING SOURCES

The KS naked singularity in Hořava's gravity has properties which distinguish it from those of the familiar Schwarzschild and Kerr solutions of GR. First, since g_{tt} at the singularity has the same value as at infinity, the singularity can be reached by a zero angular momentum test particle dropped from rest at infinity. However, if the particle loses some energy on its inbound trajectory, it will be reflected back and will oscillate between two turning points. If the energy loss continues, the particle will eventually settle at the minimum of the effective potential for radial motion of a test particle (Fig. 1), i.e., at the minimum of g_{tt} .

By the same token, since g_{tt} is finite in the neighborhood of the singularity, f being continuous, with $f(0) = 1$

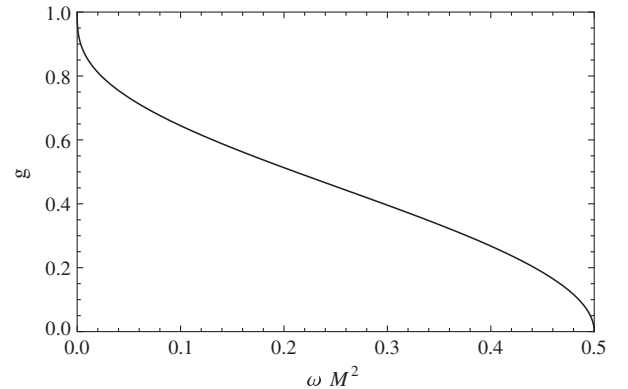


FIG. 10. Frequency shift at the surface of the antigravity sphere, at $x = x_{0G}(\omega M^2)$, Eq. (8). The Doppler frequency shift is not present here, since $\Omega(x_{0G}) = 0$. Accordingly, the shape of the line profile is unaffected, but the line is broadened and its center is shifted by the factor g , owing to gravitational redshift, Eq. (31).

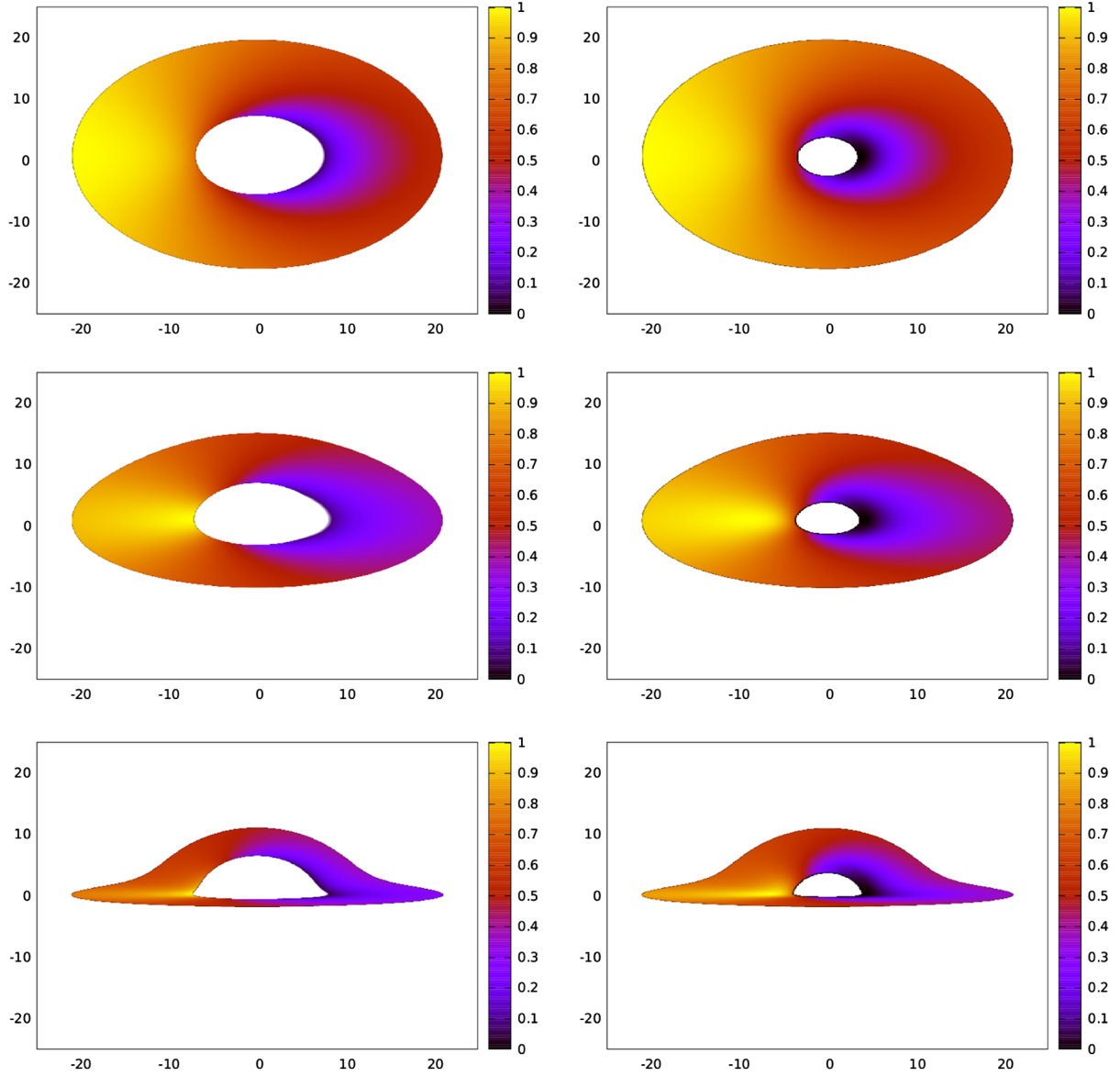


FIG. 11 (color online). Direct images of a Keplerian disk in the Schwarzschild (left) and KS metric with $\omega M^2 = 0.1$ (right). The inner radius of the disk is at $r_{\text{in}} = r_{\text{ms}}$ in the Schwarzschild case and $r_{\text{in}} = r_{\Omega\text{max}}$ in the KS case. The outer radius is $r_{\text{out}} = 20M$. Images are generated for three representative values of observer inclination $\theta_o = 30^\circ, 60^\circ$ and 85° (from top to bottom). The color scale is given by normalized frequency shift $g^* = (g - g_{\text{min}})/(g_{\text{max}} - g_{\text{min}})$.

[Eq. (6)], the effective potential for nonradial motion ($L \neq 0$) will always present an infinite centrifugal barrier, so a particle carrying any angular momentum will never reach the singularity unless it manages to lose its angular momentum without losing energy. A more likely outcome is that the particle will lose both angular momentum and kinetic energy, in which case it also can settle at the minimum of g_{tt} . In view of spherical symmetry of the KS metric, this minimum has the form of the surface of a sphere. Inside this “antigravity sphere” static observers suffer an inward radial acceleration (an outward gravitational force).

We thus come to a most interesting conclusion. Accretion of matter by the naked KS singularity will result

in accumulation of matter on the surface of a vacuum sphere around the naked singularity. Thus, an astrophysically relevant KS naked singularity will present the aspect of a spherical surface at the top of a spherical shell of accumulated matter. This sphere is likely to be quite compact. Its radius [Eq. (8)]

$$r_{0G} = \left(\frac{GM}{c^2}\right)(2\omega M^2)^{-1/3} \quad (30)$$

works out to be $r_{0G} = 150 \text{ km}$ for $\omega M^2 = 0.5 \times 10^{-3}$ and $M = 10M_\odot$. A fairly direct measurement of the Hořava parameter would be possible if spectral lines were to be

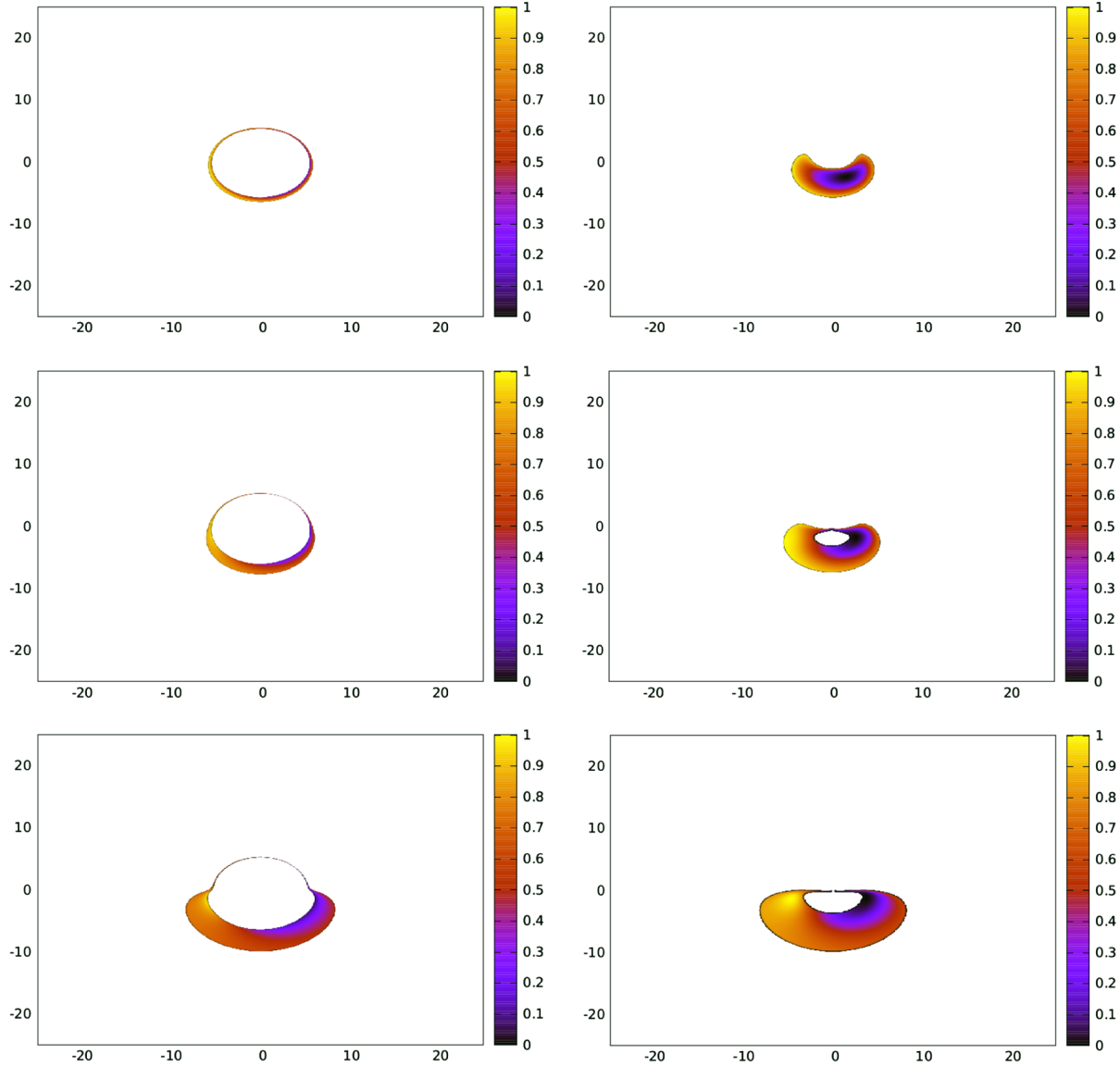


FIG. 12 (color online). First indirect images of a Keplerian disk in the Schwarzschild (left) and KS metric with $\omega M^2 = 0.1$ (right). The inner radius of the disk is at $r_{\text{in}} = r_{\text{ms}}$ in the Schwarzschild case and $r_{\text{in}} = r_{\Omega \text{max}}$ in the KS case. The outer radius is $r_{\text{out}} = 20M$. Images are generated for three representative values of observer inclination $\theta_o = 30^\circ, 60^\circ$ and 85° (from top to bottom). The color scale is given by normalized frequency shift $g^* = (g - g_{\text{min}})/(g_{\text{max}} - g_{\text{min}})$.

observed from the surface of this sphere (of radius r_{0G}). The lines would be redshifted by the amount (Fig. 10)

$$\nu_o/\nu_e = g_{tt}^{1/2} = [1 - (2\omega M^2)^{1/3}]^{1/2}. \quad (31)$$

If the naked singularity is in a binary system, it may accrete through a disk. It is thought that viscous dissipation in accretion disks is a result of the magnetorotational instability (MRI) [30], which occurs as long as angular frequency increases inwards, $d\Omega^2/dr < 0$. As we can see in Fig. 9, this would occur only down to the maximum of Ω^2 . The maximum of $\Omega^2(x)$ is rather close to the naked singularity. Indeed, for ωM^2 within 3 orders of magnitude of the black hole limit ($0.5 \times 10^{-3} < \omega M^2 < 0.5$), the

maximum is at $M < r_{\Omega \text{max}} < 16M$. In fact [31], $r_{\Omega \text{max}} = 4^{1/3}r_{0G}$.

We show sample ray-traced images of Keplerian disks in the Schwarzschild and KS metric in Figs. 11, 12, the first of which shows the direct image, while the second shows the first indirect image formed by photons which loop around the black hole/singularity before reaching the observer. The color coding reflects the redshift of the photons, Eq. (32). Overall, the direct images are not too different (between the Schwarzschild black hole and the KS naked singularity). If present, the indirect images show a greater dissimilarity. However, the major difference may be in the absence of the indirect image in the KS singularity.

For $\omega M^2 < (\omega M^2)_{\text{ms}}$ the orbits are stable down to the antigravity radius (Figs. 3, 7, 9), so in this case we would have a quasistatic fluid shell of accreted matter on the surface of the hollow (vacuum) antigravity sphere concentric with the naked singularity; a cold, probably opaque disk, abutting the sphere; and a hot accretion disk starting at a few gravitational radii (at $r_{\Omega \text{max}}$). From the astronomical point of view, this system would present an aspect quite different from a Schwarzschild or Kerr black hole. In the GR case, the Keplerian accretion disk has a hole in it (close to the ISCO) through which a second-order lensed image of the disk can be observed (inside this hole, between the ISCO and the event horizon, the fluid is optically thin owing to rapid radial inflow, e.g., [17]). In the KS singularity case, the optically thick disk would extend down to the surface of the sphere at r_{0G} , over which the fluid spreads. Thus, there would be no hole through which the strongly deflected photons responsible for the indirect image could travel towards the observer, their trajectories would intersect the opaque disk, and the right panels of Fig. 12 would have to be replaced by a blank image.

It is thought that observations of iron lines emitted by an accretion disk can be used to probe the nearly geodesic orbits of the emitting fluid [32]. We discuss the profiles of such lines in the next section.

VII. LINE PROFILES GENERATED BY ORBITAL MOTION AT ISCO AND NEAR THE ANTIGRAVITY RADIUS

We shall illustrate the potentially observable properties of the KS naked singularity spacetimes by exhibiting spectral line profiles shaped by the gravitational field and the Doppler effect related to Keplerian, i.e., geodesic circular motion.

The frequency shift $g = \nu_o/\nu_e$ of radiation emitted by a point source moving along a circular orbit in the equatorial plane and observed by a static distant observer is given by the formula

$$g = \frac{1}{u_e^t(1 - l\Omega)}, \quad (32)$$

where l is the specific angular momentum of the photon, while Ω is the angular velocity of the emitter and the temporal component of the emitter four-velocity reads

$$\frac{1}{[u_e^t]^2} = f(r) - r_e^2 \Omega^2 = 1 + r_e^2 \omega \left[1 - \sqrt{1 + \frac{4M}{r_e^3 \omega}} \right] - r_e^2 \Omega^2. \quad (33)$$

We will take Ω to be the orbital frequency of geodesic test particle motion discussed in the previous section.

The observed flux is given by $F_o = \int I_o d\Pi$, where I_o is the observed intensity and $d\Pi$ is the solid angle of the source on the observer sky. As the emitted (e) and observed

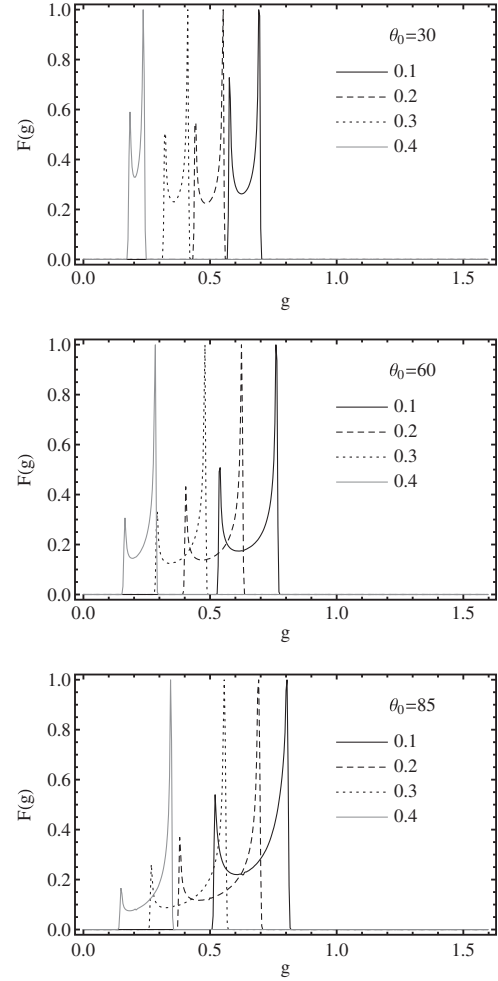


FIG. 13. Line profiles generated in Keplerian orbits at radius $x_e = 1.1x_{0G}$ for four representative values of parameter $\omega M^2 = 0.1, 0.2, 0.3, 0.4$, and three inclination angles (top to bottom) $\theta_o = 30^\circ, 60^\circ, 85^\circ$. The original emissivity function is $\epsilon(\nu) = \epsilon_o \exp[-10^{-5}(\nu/\nu_o - 1)^2]$.

(o) radiation intensities are related by the Liouville theorem $I_o/\nu_o^3 = I_e/\nu_e^3 = \text{const}$, the observed flux can be given as

$$F_o = \int I_e g^3 d\Pi. \quad (34)$$

The solid angle is expressed in terms of the coordinates α and β on the observer plane by $d\Pi = d\alpha d\beta/D_o^2$, with D_o being the distance to the source. The coordinates α and β can be then expressed in terms of the radius r_e of the orbit and the related redshift factor $g = \nu_o/\nu_e$. The corresponding Jacobian of the transformation $(\alpha, \beta) \rightarrow (r_e, g)$ then implies [33]

$$d\Pi = \frac{q}{D_o^2 \sin \theta_o \sqrt{q - \lambda^2 \cot^2 \theta_o}} \left| \frac{\partial r_e}{\partial \lambda} \frac{\partial g}{\partial q} - \frac{\partial r_e}{\partial q} \frac{\partial g}{\partial \lambda} \right|^{-1} dg dr_e. \quad (35)$$

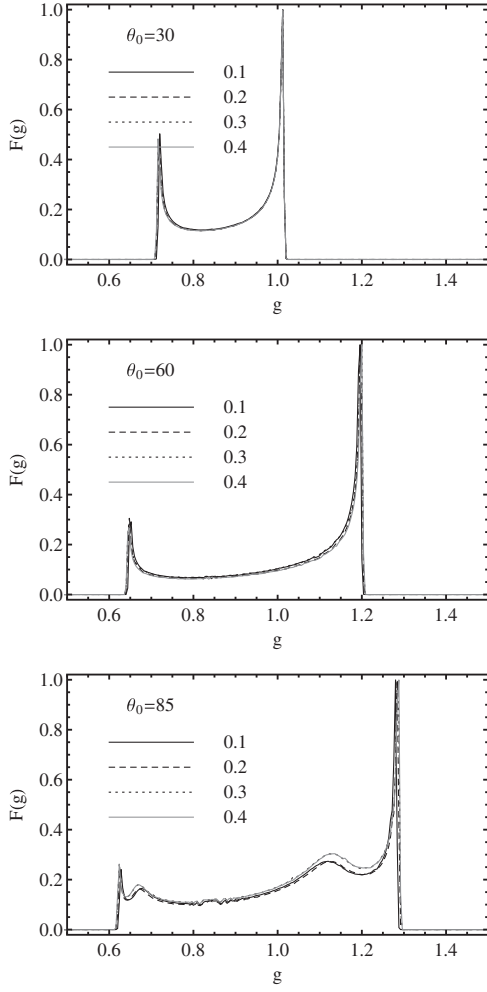


FIG. 14. Line profiles generated in Keplerian orbits at $r = 10M$ for four representative values of parameter $\omega M^2 = 0.1, 0.2, 0.3$, and 0.4 and three inclination angles (top to bottom) $\theta_0 = 30^\circ, 60^\circ$, and 85° . The original emissivity function is $\epsilon(\nu) = \epsilon_0 \exp[-10^{-5}(\nu/\nu_0 - 1)^2]$.

Here q represents the total photon impact parameter (angular momentum) and λ represents the axial impact parameter.

We calculated the profile of the spectral lines using the approach described in detail for the case of black holes in Ref. [34] and extended to the case of naked singularities in Refs. [33,35,36]. We shall not repeat the details; instead we directly present the resulting profiles of spectral lines calculated for selected characteristic positions of the Keplerian ring. The emissivity function is assumed in the form of a Gaussian curve

$$I_e(\nu_e, r_e) = I_0 \exp[-K(\nu - \nu_0)^2]. \quad (36)$$

In Fig. 10 we present the gravitational redshift of radiation of the static sources located at the antigravity radius x_{0G} , Eq. (8), which directly demonstrates a fundamental property of the naked singularity in the KS

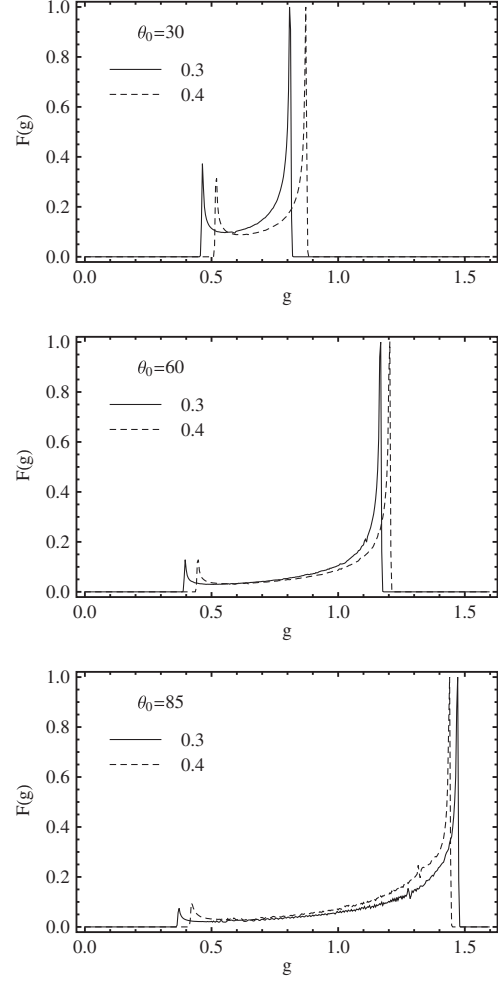


FIG. 15. Line profiles generated at ISCO for two values of parameter $\omega M^2 = 0.3$, and 0.4 , and three inclination angles $\theta_0 = 30^\circ, 60^\circ$, and 85° . The original emissivity function is $\epsilon(\nu) = \epsilon_0 \exp[-10^{-5}(\nu/\nu_0 - 1)^2]$.

spacetime, the presence of the antigravity sphere. Here, the gravitational redshift increases with increasing values of the spacetime parameter ωM^2 . “Circular” geodesics at $x = x_{0G}$ correspond to zero velocity, so there is no Doppler shift; the lines are redshifted with no change of profile.

In Fig. 13 we give the spectral line profiles observed at infinity for Keplerian rings located slightly above the static radius, at $x = 1.1x_{0G}$, for four characteristic values of the parameter ω and three characteristic values of the inclination angle between the ring and the distant observer $\theta_0 = 30^\circ, 60^\circ, 85^\circ$. The characteristic double-horned profile is caused by the orbital Doppler shift. We clearly observe the increasing redshift of the line as the value of the spacetime parameter ωM^2 increases. The width of the line increases with increasing inclination angle θ_0 . However the Doppler blueshift never dominates over the gravitational redshift in this figure; all parts of the profile are redshifted. However, if this part of the disk is cold, the lines presented in Fig. 13 may not be detectable.

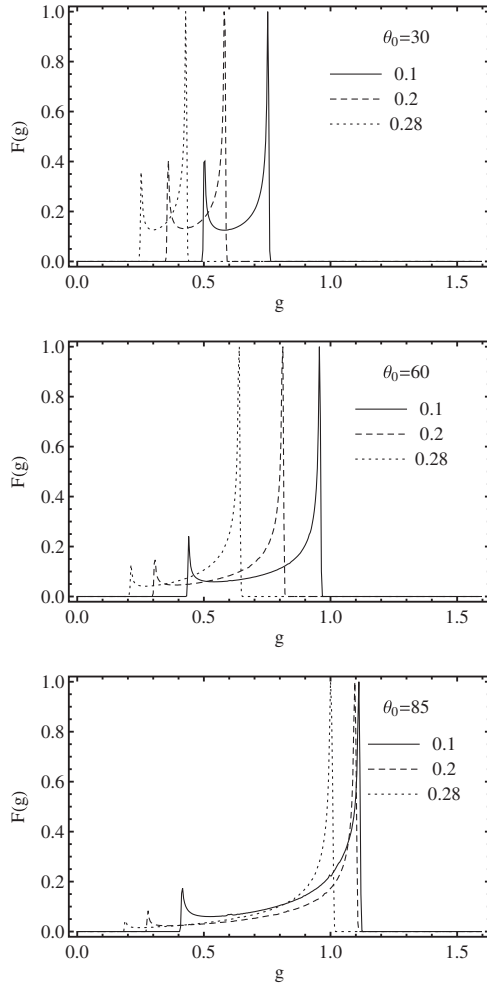


FIG. 16. Line profiles generated at radius $r_e = r_{\Omega \max}$ for three representative values of parameter $\omega M^2 = 0.1, 0.2, 0.28$, and three inclination angles $\theta_0 = 30^\circ, 60^\circ, 85^\circ$. The original emissivity function is $\epsilon(\nu) = \epsilon_0 \exp[-10^{-5}(\nu/\nu_0 - 1)^2]$.

Similar effects are demonstrated in Fig. 14 also for the Keplerian rings located at $r = 10M$, where the line profiles coincide for all the characteristic values of the spacetime parameter ωM^2 . For large inclination angle, the line profiles become more complex than for the other cases, as additional small maxima of the profiles arise in such a situation.

In Fig. 15 we present the line profiles generated by Keplerian rings located at the ISCO orbits for the KS naked singularity spacetimes with $\omega M^2 = 0.3, 0.4$. Now the role of the inclination angle is of paramount importance, the line profiles are extended, and the blue wing has relatively large $g \sim 1.5$ for large inclination angles. For comparison we give in Fig. 16 the line profiles generated by Keplerian rings at the radius $r_e = r_{\Omega \max}$ where the radial profile of the angular velocity of the Keplerian motion reaches its maximal value. The effects of these parameters are of the same character as for rings close to $x = x_{\text{OG}}$, but they are amplified by the stronger effect of the Doppler shift. Therefore, the redshifted end is lowered and shifted to lower values of g ,

while the blueshifted end is increased and shifted to larger values of g ; for large inclination angles this leads to $g > 1$ in the blue edge. Note that the lines at $r_{\Omega \max}$ have a clearly smaller blueshift than the lines formed at the ISCO.

We can conclude that the spectral line profiles generated by Keplerian rings could demonstrate a clear signature of the presence of the KS naked singularities and could enable measurement of the parameter ω , if the inclination angle were known. An extended study of the optical effects related to the KS naked singularity spacetimes can be found in [31,37].

VIII. CONCLUSIONS

We discussed photon and test-particle orbits in the Kehagias-Sfetsos metric as a function of the Hořava parameter times mass squared, ωM^2 . The parameter ω is assumed to be a universal constant with a fixed value which is not known at the present time. The current best constraint $\omega > 3.2 \times 10^{-20} \text{ cm}^{-2}$ [12] implies that the so-called supermassive black holes ($M \geq 10^5 M_\odot$) observed in the centers of galaxies would indeed be black holes in the KS metric. However, stellar-mass black hole candidates, if described by the KS metric, could be either black holes or naked singularities under the current lower limit on ω .

For naked singularities there are three different regimes of circular motion, depending on the value of M . There is always an “antigravity sphere” on whose surface a test particle can remain at rest (in a zero angular momentum geodesic), and inside which no circular geodesics exist. For low values of the mass, circular motion is possible everywhere outside the antigravity sphere and is always stable. For intermediate mass values, there are two distinct regions of stable circular motion—the inner one terminates in an OSCO and the outer one begins in an ISCO—the two regions are separated by a region where circular orbits are unstable. For the largest values of M compatible with the existence of a naked singularity there is an inner region of stable timelike circular geodesics, terminated by a stable photon orbit, and an outer region of stable circular geodesics beginning with an ISCO. Between the stable photon orbit and the ISCO there are two regions separated by an unstable circular photon orbit: in the inner one no circular orbits are allowed, and in the outer one circular timelike geodesics are unstable (Fig. 3). The KS metric is static, and this is the only one we have considered. In GR it is known that the properties of orbits for rotating naked singularities differ from those of the static ones [38].

The properties of circular orbits of the Kehagias-Sfetsos and the Reissner-Nordström naked singularities are qualitatively similar (cf., this work and [24,25]), but very different from the black hole ones. When event horizons are present, the orbits outside the black hole are qualitatively similar to those of the Schwarzschild metric. No circular geodesics exist between the singularity and the inner horizon.

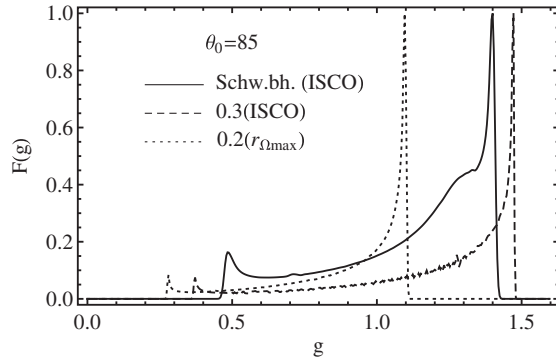


FIG. 17. Comparison of spectral line profiles generated from a Keplerian ring at the ISCO of a Schwarzschild black hole (solid), the ISCO of a KS naked singularity with parameter $\omega M^2 = 0.3$ (dashed) and at the orbit of maximum angular velocity (at $r = r_{\Omega \max}$) of a KS naked singularity with parameter $\omega M^2 = 0.2$ (dotted). Observer inclination is $\theta_o = 85^\circ$.

The differences between the KS naked singularity and GR black hole cases should have astrophysical consequences. For instance, the line profiles in the KS naked singularity metric are different from those obtained for geodesic motion in the Schwarzschild metric. In Fig. 17 we compare the line profiles generated by orbital motion in the ISCO of a KS singularity ($\omega M^2 = 0.3$) and of the Schwarzschild metric. We see that in the former case the gravitational well is more shallow, resulting in a smaller redshift of the line than in the Schwarzschild case. As discussed above, in the KS metric corresponding to a

naked singularity, unlike in the Schwarzschild metric, the angular frequency of stable circular test particle orbits may attain a maximum in an orbit which does not correspond to the ISCO (Fig. 9). The line profile corresponding to that orbit, at $r_{\Omega \max}$ for $\omega M^2 = 0.2$, is also presented in Fig. 17.

Perhaps the most distinctive property of KS naked singularity is the presence of an “antigravity” sphere where any accreted fluid may rest in equilibrium, any emission from that spherical shell will be redshifted by a definite factor which is a function of ωM^2 alone (Fig. 10).

These considerations suggest that stringent constraints might be placed on the Hořava parameter through observation of astrophysical black holes. If the galactic soft x-ray transients were found to indeed contain a black hole (and not a naked singularity), the lower limit on ω would be increased by 7 orders of magnitude (relative to the best current limits) to $\omega > 2.2 \times 10^{-13} \text{ cm}^{-2}$ for a $10M_\odot$ black hole.

ACKNOWLEDGMENTS

This work supported in part by Brazilian grant from “Fundação de Amparo à Pesquisa do Estado de São Paulo (FAPESP),” Grant No. 2013/01001-0, Czech Grant No. CZ.1.07/2.3.00/20.0071 “Synergy” and Polish NCN Grants No. 2013/08/A/ST9/00795 and No. 2011/01/B/ST9/05439. J. S. and Z. S. acknowledge the Albert Einstein Center for Gravitation and Astrophysics, Czech Science Foundation Grant No. 14-37086G.

-
- [1] P. Hořava, *Phys. Rev. D* **79**, 084008 (2009).
 - [2] P. Hořava, *Phys. Rev. Lett.* **102**, 161301 (2009).
 - [3] P. Hořava and Ch. M. Melby-Thompson, *Phys. Rev. D* **82**, 064027 (2010).
 - [4] T. Griffin, P. Hořava, and Ch. M. Melby-Thompson, *Phys. Rev. Lett.* **110**, 081602 (2013).
 - [5] A. Kehagias and K. Sfetsos, *Phys. Lett. B* **678**, 123 (2009).
 - [6] V. Enolskii, B. Hartmann, V. Kagramanova, J. Kunz, C. Lämmerzahl, and P. Sirimachan, *Phys. Rev. D* **84**, 084011 (2011).
 - [7] T. Harko, Z. Kovács, and F. S. N. Lobo, *Classical Quantum Gravity* **28**, 165001 (2011).
 - [8] K. Yagi, D. Blas, E. Barausse, and N. Yunes, *Phys. Rev. D* **89**, 084067 (2014).
 - [9] L. Iorio and M. L. Ruggiero, *Int. J. Mod. Phys. A* **25**, 5399 (2010).
 - [10] M. Liu, J. Lu, B. Yu, and J. Lu, *Gen. Relativ. Gravit.* **43**, 1401 (2011).
 - [11] T. Harko, Z. Kovács, and F. S. N. Lobo, *Proc. R. Soc. A* **467**, 1390 (2011).
 - [12] L. Iorio and M. L. Ruggiero, *Int. J. Mod. Phys. D* **20**, 1079 (2011).
 - [13] N. I. Shakura and R. A. Sunyaev, *Astron. Astrophys.* **24**, 337 (1973).
 - [14] I. D. Novikov and K. S. Thorne, in *Black Holes*, edited by C. DeWitt and B. S. DeWitt (Gordon & Breach, New York, 1973), p. 345.
 - [15] W. Kluźniak, P. Michelson, and R. V. Wagoner, *Astrophys. J.* **358**, 538 (1990).
 - [16] M. A. Abramowicz and W. Kluźniak, *Astrophys. Space Sci.* **300**, 127 (2005).
 - [17] A. Sądowski, M. Abramowicz, M. Bursa, W. Kluźniak, J.-P. Lasota, and A. Różańska, *Astron. Astrophys.* **527**, A17 (2011).
 - [18] M. Bursa, M. A. Abramowicz, V. Karas, W. Kluźniak, and A. Schwarzenberg-Czerny, *RAGtime 8/9: Workshops on Black Holes and Neutron Stars*, edited by S. Hledík and Z. Stuchlík (Silesian University, Opava, 2007).
 - [19] K. Fukumura, D. Kazanas, and G. Stephenson, *Astrophys. J.* **695**, 1199 (2009).
 - [20] J. Chen and Y. Wang, *Int. J. Mod. Phys. A* **25**, 1439 (2010).

- [21] A. Abdujabbarov, B. Ahmedov, and A. Hakimov, *Phys. Rev. D* **83**, 044053 (2011).
- [22] M. Dwornik, Zs. Horváth, and L. Á. Gergely, *Astron. Nachr.* **334**, 1039 (2013).
- [23] Z. Kovács and T. Harko, *Phys. Rev. D* **82**, 124047 (2010).
- [24] Z. Stuchlík and S. Hledík, *Acta Phys. Slovaca* **52**, 363 (2002).
- [25] D. Pugliese, H. Quevedo, and R. Ruffini, *Phys. Rev. D* **83**, 024021 (2011).
- [26] K. Goluchová, K. Kulczycki, R. S. S. Vieira, Z. Stuchlík, W. Kluźniak, and M. Abramowicz (unpublished).
- [27] Shi-Wei Zhou and Wen-Biao Liu, *Int. J. Theor. Phys.* **50**, 1776 (2011).
- [28] P. S. Letelier, *Phys. Rev. D* **68**, 104002 (2003).
- [29] A. García, E. Hackmann, J. Kunz, C. Lämmerzahl, and A. Macias, [arXiv:1306.2549v3](#).
- [30] S. A. Balbus and J. F. Hawley, *Rev. Mod. Phys.* **70**, 1 (1998).
- [31] Z. Stuchlík and J. Schee, [arXiv:1402.2891](#).
- [32] G. Matt, A. C. Fabian, and R. R. Ross, *Mon. Not. R. Astron. Soc.* **278**, 1111 (1996).
- [33] J. Schee and Z. Stuchlík, *J. Cosmol. Astropart. Phys.* **4** (2013) 005.
- [34] J. Schee and Z. Stuchlík, *Gen. Relativ. Gravit.* **41**, 1795 (2009).
- [35] Z. Stuchlík and J. Schee, *Classical Quantum Gravity* **27**, 215017 (2010).
- [36] Z. Stuchlík and J. Schee, *Classical Quantum Gravity* **30**, 075012 (2013).
- [37] Z. Stuchlík, J. Schee, and A. Abdujabbarov, *Phys. Rev. D* **89**, 104048 (2014).
- [38] Z. Stuchlík, *Bull. Astron. Inst. Czech.* **31**, 129 (1980).